



**National Ignition Facility Target Area
Studies Final Report for the Period
4/1/96 through 11/30/96**

R.R. Peterson, J.F. Santarius, G.A. Moses

January 1997

UWFDM-1036

FUSION TECHNOLOGY INSTITUTE

UNIVERSITY OF WISCONSIN

MADISON WISCONSIN

DISCLAIMER

This report was prepared as an account of work sponsored by an agency of the United States Government. Neither the United States Government, nor any agency thereof, nor any of their employees, makes any warranty, express or implied, or assumes any legal liability or responsibility for the accuracy, completeness, or usefulness of any information, apparatus, product, or process disclosed, or represents that its use would not infringe privately owned rights. Reference herein to any specific commercial product, process, or service by trade name, trademark, manufacturer, or otherwise, does not necessarily constitute or imply its endorsement, recommendation, or favoring by the United States Government or any agency thereof. The views and opinions of authors expressed herein do not necessarily state or reflect those of the United States Government or any agency thereof.

**National Ignition Facility Target Area Studies
Final Report for the Period 4/1/96 through 11/30/96**

Robert R. Peterson, John F. Santarius, Gregory A. Moses

Fusion Technology Institute
University of Wisconsin-Madison
1500 Engineering Drive
Madison, WI 53706

January 1997

UWFDM-1036

1. Introduction

During the period 4/1/96 through 11/30/96, progress was made on the study of target chamber phenomena in the National Ignition Facility (NIF) in the study of material response to debris, in the development of a 2-D radiation hydrodynamics code and in additional verification of the BUCKY code [1]. This work follows work reported earlier [2], which covered accomplishments between 5/1/95 and 3/31/96. Some aspects of this work were reported upon at the 1996 American Nuclear Society meeting [3, 4, 5], and at the 1996 American Physical Society Division of Plasma Physics meeting [6].

The NIF target area is shown in Figure 1. The general features of the target chamber are listed in Table 1. The debris spectrum from a 40 MJ yield direct drive target is shown in Table 2. The energy partitioning from direct and indirect drive NIF targets are shown in Table 3. The first wall is coated with one of several possible materials. The three most likely materials are shown in the table. The coating is on a substrate of aluminum alloy, which is the structural material for the target chamber. The coating must undergo only a minimal amount of vaporization and melting from the x-rays and debris from any likely target explosion. The material that is lost from the target chamber walls could deposit onto the debris shields that protect the laser optics, requiring cleaning. Energetic tritium ions from the targets will penetrate the surface of the coatings and the debris shield, leading to a growing radioactive inventory that can be controlled through periodic cleaning by removal of the surface layers. The work discussed in this report addresses these issues and the development and testing of computer models for their study.

In this report, we will report on progress in the following areas:

- Recalculation of tritium deposition with continuous energy spectrum.
- Verification of the radiation transport in the BUCKY computer code with x-ray burnthrough experiments.
- ZEUS-2D continued development and verification.
- Experiments underway at Sandia National Laboratories to verify ion melting calculations in BUCKY.

Table 1. NIF Target Area Parameters

First Wall Radius (m)	5
First Wall Material	Aluminum Alloy
First Wall Coating	Plasma Sprayed B ₄ C, Plasma Sprayed Al ₂ O ₃ , Carbon/Carbon Composite
Optical Material	SiO ₂
Target Chamber Atmosphere	Vacuum

Table 2. Direct Drive Target Debris Energy Spectrum

Bin #	1	2	3	4	5	6	7
Species	T	T	T	D	D	D	C
Velocity (cm/ns)	0.13	0.20	0.27	0.13	0.20	0.27	0.5
Energy (keV)	26.4	62.5	114	17.6	41.7	76	3130
# of ions ($\times 10^{19}$)	4.77	12.3	4.77	4.77	12.3	4.77	.452
Start of Pulse at 5 m (μ s)	3.03	2.13	1.67	3.03	2.13	1.67	.980
End of Pulse at 5 m (μ s)	5.00	3.03	2.13	5.00	3.03	2.13	1.02
Pulse Width at 5 m (μ s)	1.97	0.9	0.46	1.97	0.9	0.46	0.04
Pulse Energy (MJ)	0.202	1.30	0.871	0.135	0.865	0.58	2.26
Power (TW)	0.103	1.44	1.89	0.069	0.961	1.26	56.5

Table 3. Target Energy Balance

	Direct Drive		Indirect Drive	
	Pure DT	CH Coated	Ignited	Significant Yield
E_{laser}	1.26	1.27	1.31	1.33
TN Yield (MJ)	38.6	39.7	0.11	9.40
Neutron Losses (MJ)	32.4	33.1	0.08	7.12
X-ray Losses (MJ)	0.38	0.40	0.45	1.98
Debris Energy (MJ)	7.04	7.44	0.89	1.63
Max. Total Energy (MJ)	39.8	41.0	1.42	10.73

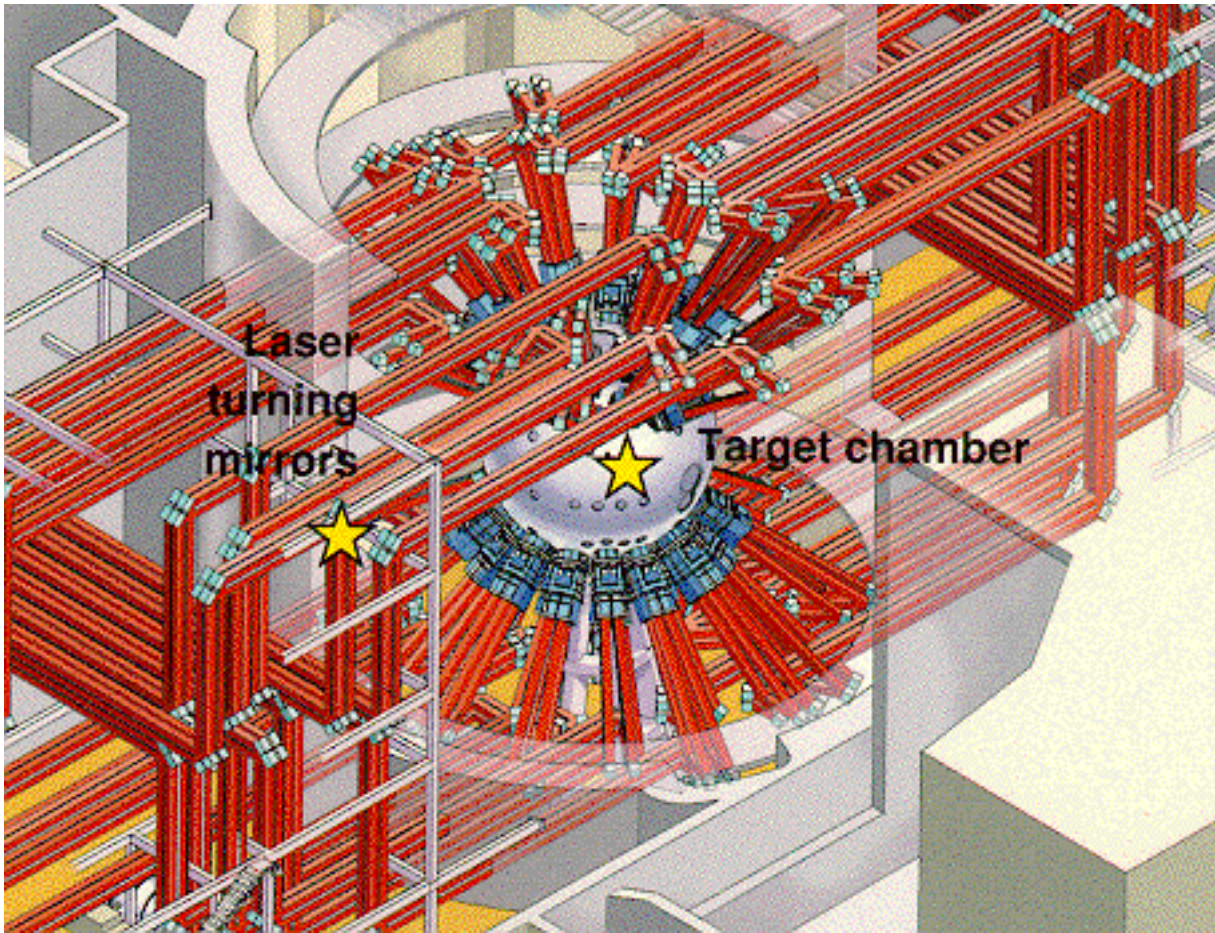


Figure 1. Schematic picture of NIF target area.

2. Tritium Deposition Calculations

The deposition of tritium was calculated and reported on in the interim report [2] for a discrete energy spectrum. In the meantime, new calculations have been performed, where the tritium energy spectrum is continuous. The result is that the tritium deposition profiles are smoothly distributed in the absorbing medium. Another minor correction has been made to the ion stopping power calculation in BUCKY, which makes little difference to the tritium range.

BUCKY considers the effects of free electron, bound electrons and target nuclei in the calculation of ion stopping. The traditional approach in BUCKY has been to divide the contributions from free and bound electrons and treat them separately. In the calculations presented in this section, this approach is used. In this work, free electrons in the stopping

medium are not important because the medium never gets hot enough to do much ionization. The bound electron contribution is calculated in two ways, depending on the ion energy. At low energy, the Lindhard-Scharff [7] model is used. Here, the stopping power is calculated as,

$$\left(\frac{dE}{dx}\right)_{LS} = (3.84 \times 10^{18} \text{ keV cm}^{-1}) N_2 \frac{Z_1^{7/6} Z_2^*}{[Z_1^{2/3} + (Z_2^*)^{2/3}]^{3/2}} \left(\frac{E_1}{A_1}\right)^{1/2}. \quad (1)$$

Here, Z_1 , E_1 , and A_1 are respectively the atomic number, energy in keV, and atomic mass of the projectile ions. Z_2^* is the average number of bound electrons per atom in the stopping medium. When BUCKY calculates the stopping in solid or liquid media, it assumes that $Z_2^* = 0$. This expression is valid when the velocity of the projectile ions is small compared to the orbital velocities of the bound electrons in the stopping medium. Here the stopping power is proportional to the projectile ion velocity. This expression derives from the treatment of the electrons in the stopping medium as a cloud.

When the velocity of the projectile ions is greater than the orbital velocities of electrons in the stopping medium, BUCKY uses the Bethe [8] stopping power;

$$\left(\frac{dE}{dx}\right)_{Bethe} = \left(\frac{\omega_p q_1 e}{v_1}\right)^2 \left[\ln \left(\frac{2m_e v_1^2}{\langle \Phi_2 \rangle (1 - v_1^2/c^2)} \right) - \frac{v_1}{c} \right]. \quad (2)$$

Here, ω_p and $\langle \Phi_2 \rangle$ are the electron plasma frequency and the average ionization potential in the stopping medium. q_1 and v_1 are the projectile ion charge state and velocity. The Bethe model treats the bound electrons in the stopping medium as point charges. In this expression, the stopping power decreases with increasing projectile velocity.

Since the Lindhard model predicts increasing stopping power at low ion energy and the Bethe model predicts a falling stopping power at high ion energies, a maximum exists in the interface between the regions of validity of the two models. This is when the projectile ion velocity is approximately equal to the orbital velocity of the bound electrons in the stopping medium. BUCKY does a linear interpolation between these two methods in this regime. A new feature in BUCKY allows a more general calculation of the stopping power, where the interaction of bound electrons in a muffin-tin potential is explicitly calculated [9]. This gives the same results as the Lindhard model at low ion energies and the Bethe model at high energy, but it is a better approach in this intermediate region. The range calculated has been compared with calculations of the TRIM [10] code that uses fits to experimental data.

The results of the BUCKY tritium deposition calculations are shown in Figures 2 through 4. BUCKY records the positions where ions deposit in the solid materials. The density of tritium ions is plotted against distance into the material. The tritium energy spectrum for 40 MJ direct drive targets is obtained from the mass density and velocity profiles shown in Figure 5. The tritium energies from 40 MJ direct drive targets range from 25 keV to 115 keV. For 100 kJ, the ion energies are scaled down to the range of 0.9 keV to 4 keV. It is difficult to predict the tritium energies from an indirect drive NIF target. Lagrangian hydrodynamic simulations predict that the tritium is largely trapped behind the mass of the outer parts of the target, but the hydrodynamic stability of the target during breakup has not been studied. If total laser entrance hole closure is assumed and hydrodynamic stability is ignored, a 12 MJ indirect drive target generates 1 keV tritiums.

BUCKY calculations were performed for both direct and indirect drive tritium spectra and for penetration into boron and SiO₂. The fluences of particles are calculated from the target mass and the distance to the first wall (5 m). The ions stop where they run out of energy in the dE/dx calculation in BUCKY described above and the ion density profiles for a single shot are calculated and plotted. No migration of the ions after they stop is included. The temperature profiles in materials are calculated and migration rates could be estimated if the diffusivity of tritium in the material as a function of temperature was known.

The results of these calculations indicate that for both of the materials studied, tritium will penetrate no more than about 2 μm into the material. For indirect drive targets, the ion energy is low so the tritiums only penetrate a few tenths of a micron. 40 MJ direct drive targets have much higher tritium energies so the tritium ions penetrate deeper into the materials, while the low yield direct drive targets penetrate ions to similar depths as the indirect drive targets. These results are dependent on the debris spectrum, which has the uncertainties suggested above.

3. Verification of the Radiation Transport in the BUCKY Computer Code with X-ray Burnthrough Experiments

The BUCKY code has been compared with radiation burnthrough experiments performed on the Nova laser at LLNL [11]. In these experiments, x rays produced in a gold hohlraum with the Nova laser beams are allowed to burn through a thin gold foil. The hohlraums are cylinders 0.16 cm in diameter and 0.275 cm long with walls 25 μm thick. Gold foils and observation holes are placed in the hohlraum walls near the center. Ten laser beams

Tritium Density in Boron

Single direct drive shot; 5 m from target

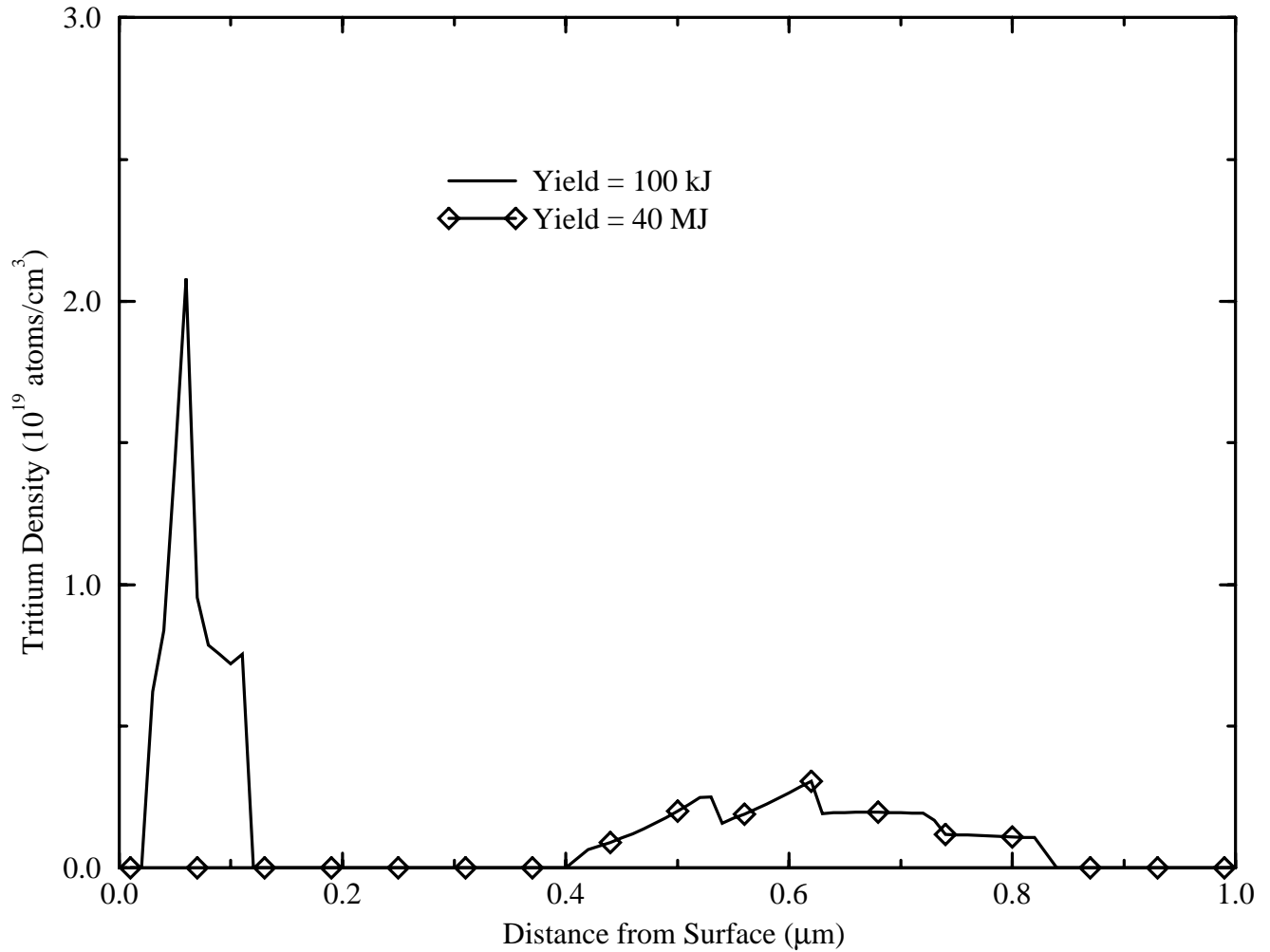


Figure 2. BUCKY simulation of the deposition of tritium from a 40 MJ and 100 kJ direct drive NIF target into 2.375 g/cm³ boron. A continuous tritium energy spectrum is estimated from the velocity and density profiles.

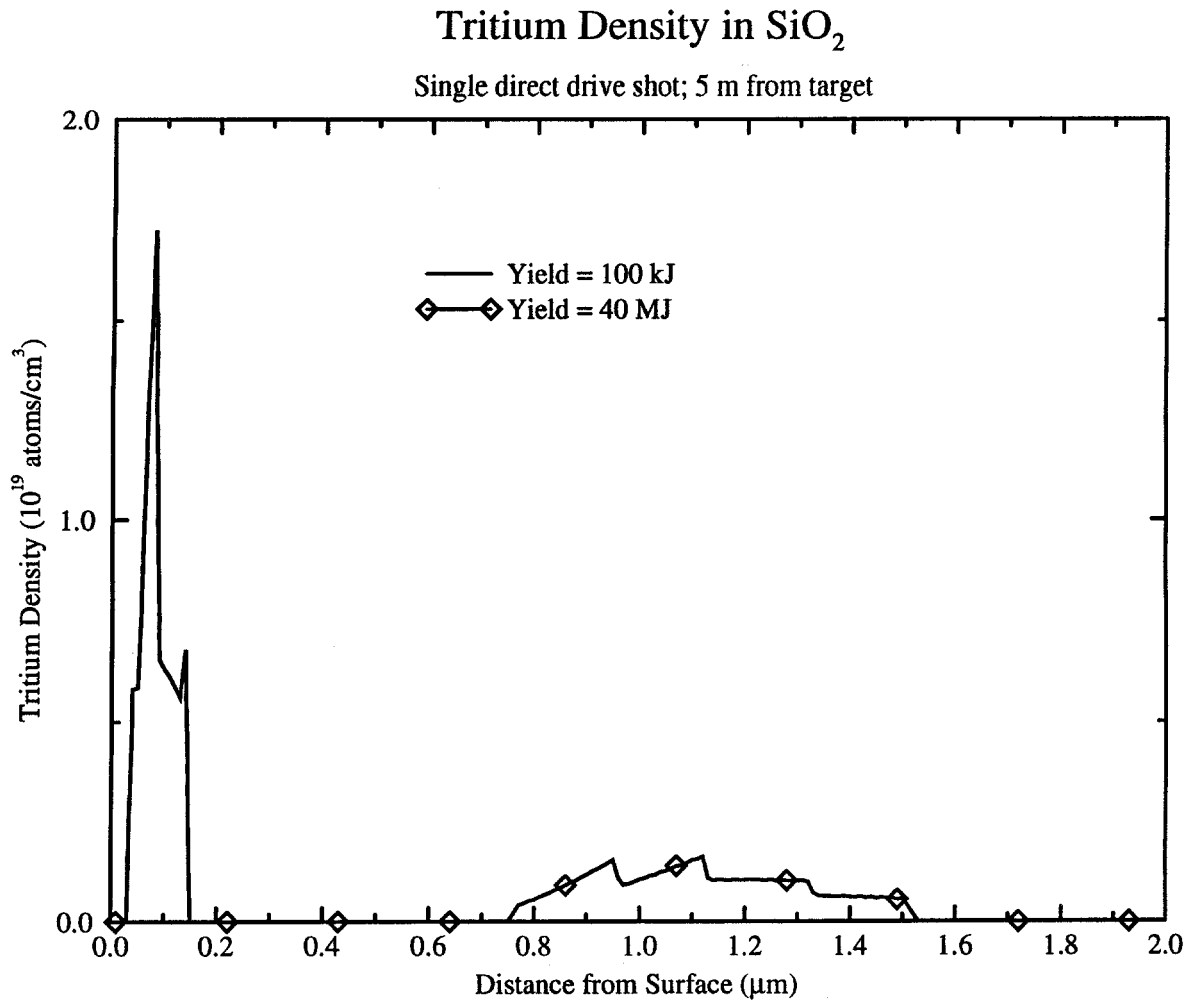


Figure 3. BUCKY simulation of the deposition of tritium from a 40 MJ and 100 kJ direct drive NIF target into 2.26 g/cm³ SiO₂. A continuous tritium energy spectrum is estimated from the velocity and density profiles.

Tritium Density in Wall Material

Single indirect drive 12 MJ shot; 5 m from target

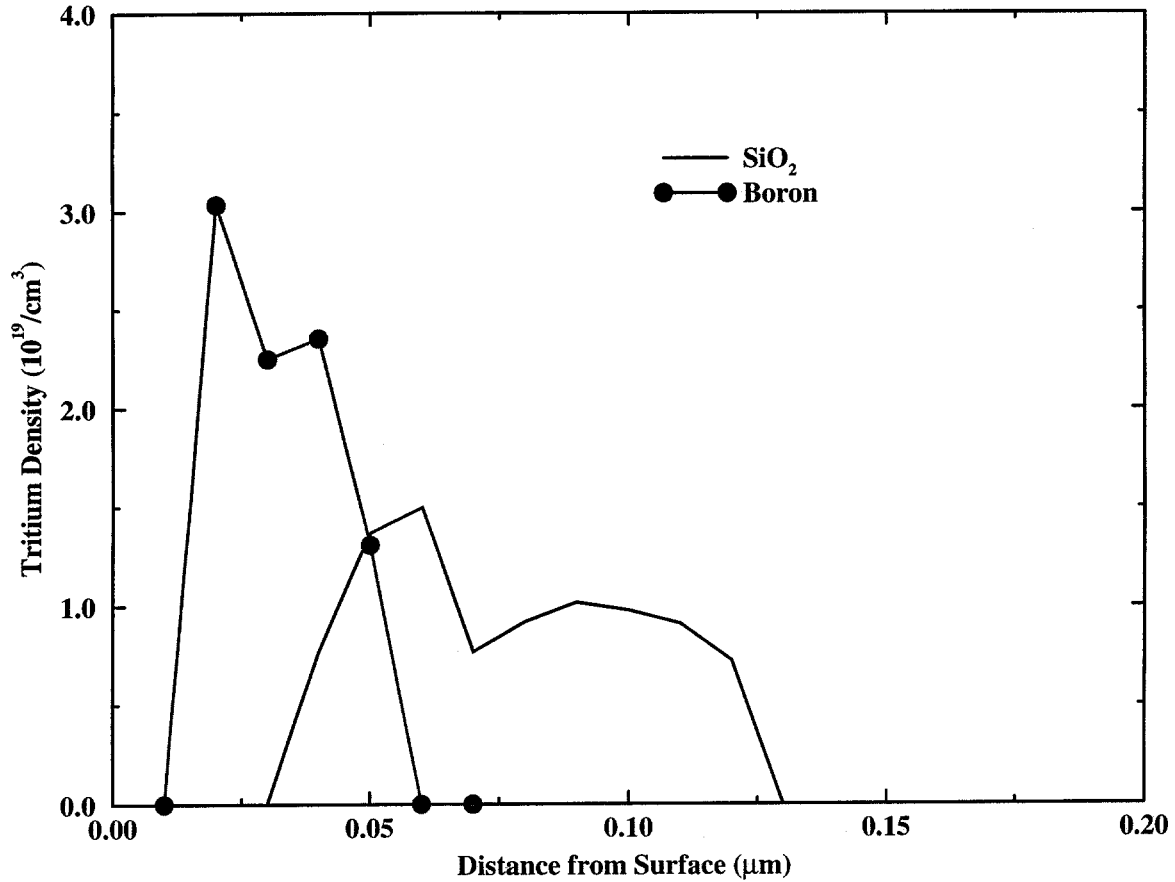


Figure 4. BUCKY simulation of the deposition of tritium from a 12 MJ indirect drive NIF target into 2.375 g/cm³ boron and 2.26 g/cm³ SiO₂. A continuous tritium energy spectrum is estimated from the velocity and density profiles.

BUCKY Simulation of NIF Direct-Drive Target

10 ns after end of burn

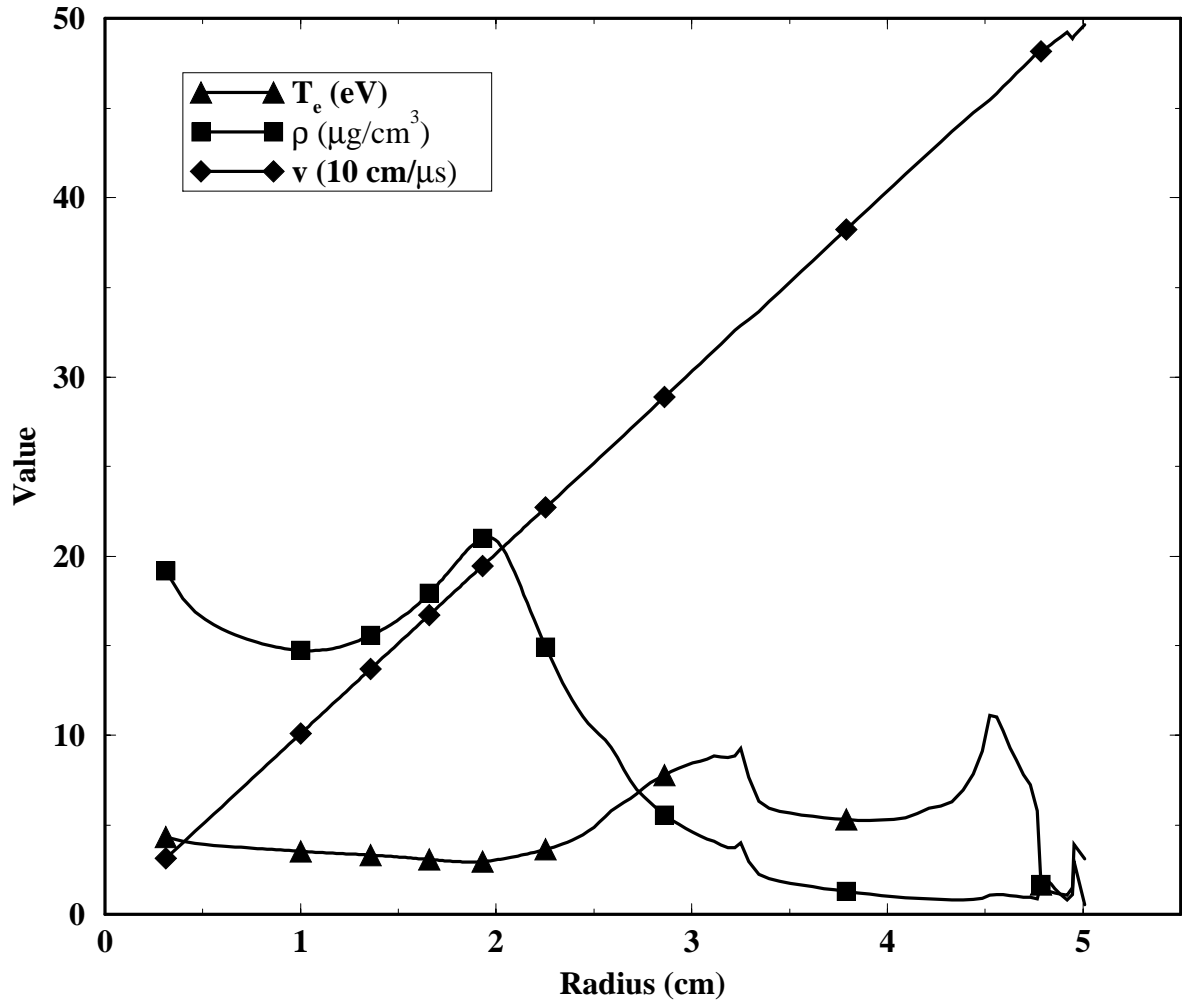


Figure 5. BUCKY simulation of the break-up of a NIF direct drive target. Velocity, mass density and temperature profiles are shown at 10 ns after end of burn.

enter the hohlraums through holes at each end of the cylinder and shine on the inside of the walls. The laser pulse shape is assumed to be trapezoidal, with a 0.8 ns flat top. The x rays create a Marshak wave in the gold, whose speed is a function of the opacity and equation of state of the gold. The transit time of the Marshak wave is measured for foil thicknesses from 1 to 3 μm by observing the history of the x-ray emissions from the back of the foils with a Streaked X-ray Imager (SXI). Simultaneously, the drive radiation inside the hohlraum is measured with the DANTE x-ray diode array. DANTE observes the x-ray power emitted by a given array on the inside of the hohlraum wall in several energy channels. This can be converted into an effective wall temperature, that is reported as a function of time [11].

These experiments have been modeled with the BUCKY code in 1-D. The Nova hohlraum is modeled as two slabs of solid gold separated by 0.15 cm of low density gold vapor, as shown in Figure 6. BUCKY models the deposition of the laser in the vapor and on the inside edge of one of the walls, assuming that the beams are incident at 45° . Radiation transport is modeled with 100 energy group flux-limited diffusion. Equations-of-state come from SESAME tables [12], and opacities from tables generated with the EOSOPA code [13], where the UTA method is used to calculate high atomic number opacities.

The proper intensity of the laser is uncertain, because in a hohlraum the lasers are focused in distinct spots which is a 3-D problem. The intensity has been varied until the code predicts the wall temperature measured by DANTE. The wall temperature is calculated as the blackbody temperature that would create the emitted flux predicted by the BUCKY simulations. The simulations used flux limited diffusion for the radiation transport, which only provides the net flux across the wall surface, so the emitted flux is calculated as the difference between the net flux and the flux from the center of the hohlraum, σT_r^4 (center). The radiation temperature in the center of the hohlraum or drive temperature, calculated wall temperature, and the DANTE measured wall temperature are plotted in Figure 7 for a laser intensity of $150 \text{ TW}/\text{cm}^2$. One can see that this intensity is close to agreeing with the DANTE measurements.

Using $150 \text{ TW}/\text{cm}^2$ as a laser intensity, the burnthrough of various thicknesses of the gold foils has been simulated with BUCKY. The burnthrough time is defined as the time between when the drive flux reaches 10% of its maximum and when the flux at the back of the foil reaches 50% of its peak. The SXI measures the flux in channels between 210 and 240 eV and 430 and 570 eV. BUCKY group structure allows channels between 208 and 236 eV and 451 and 547 eV. The comparisons of the burnthrough times for radiation in these channels are shown in Figure 8, plotted against foil thickness. One can see that the BUCKY

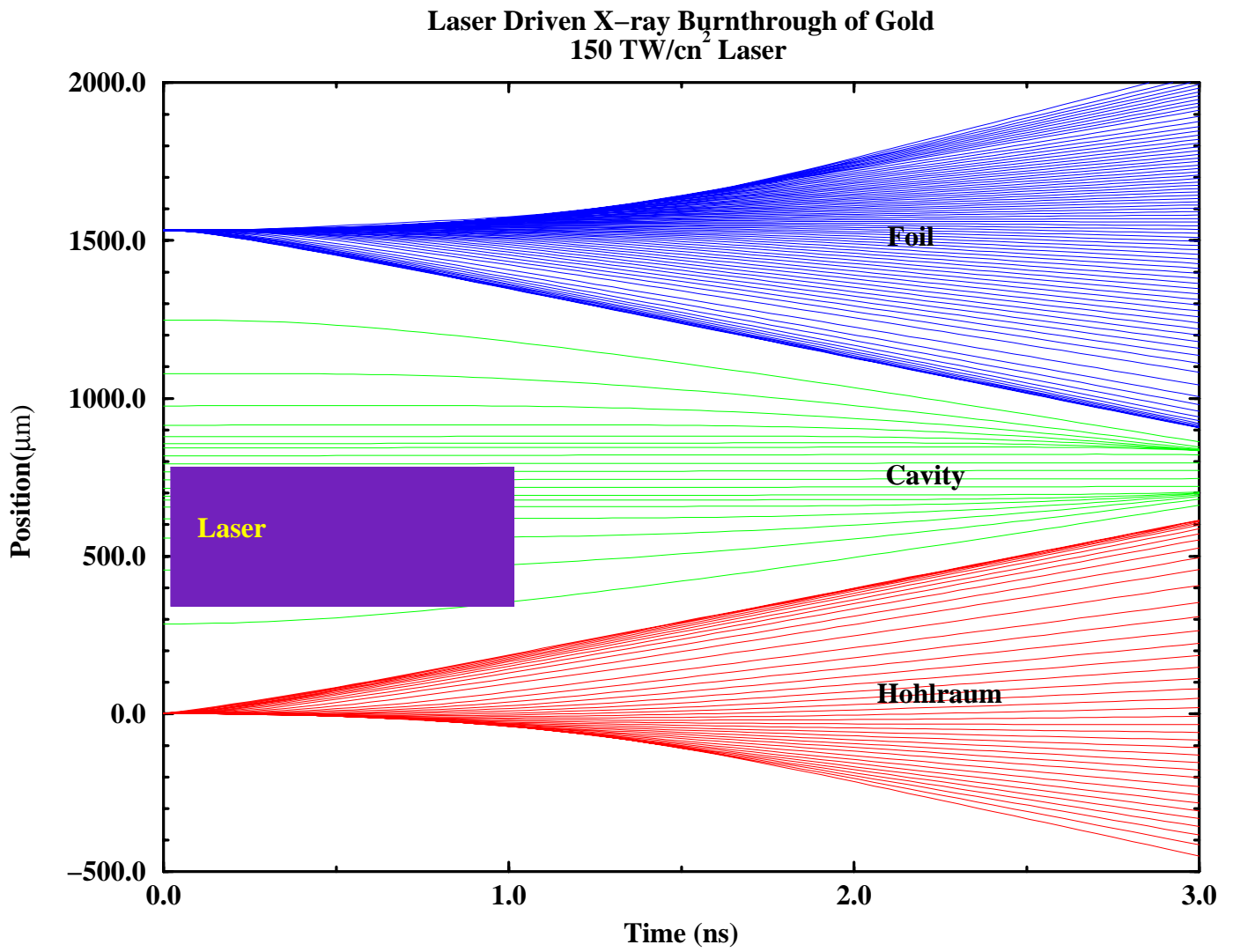


Figure 6. Positions of Lagrangian zone boundaries versus time in BUCKY simulation of Nova gold burnthrough experiment.

Wall Temperature at Drive Surface

Gold Foil Driven by X Rays Produced by 150 TW/cm² Laser

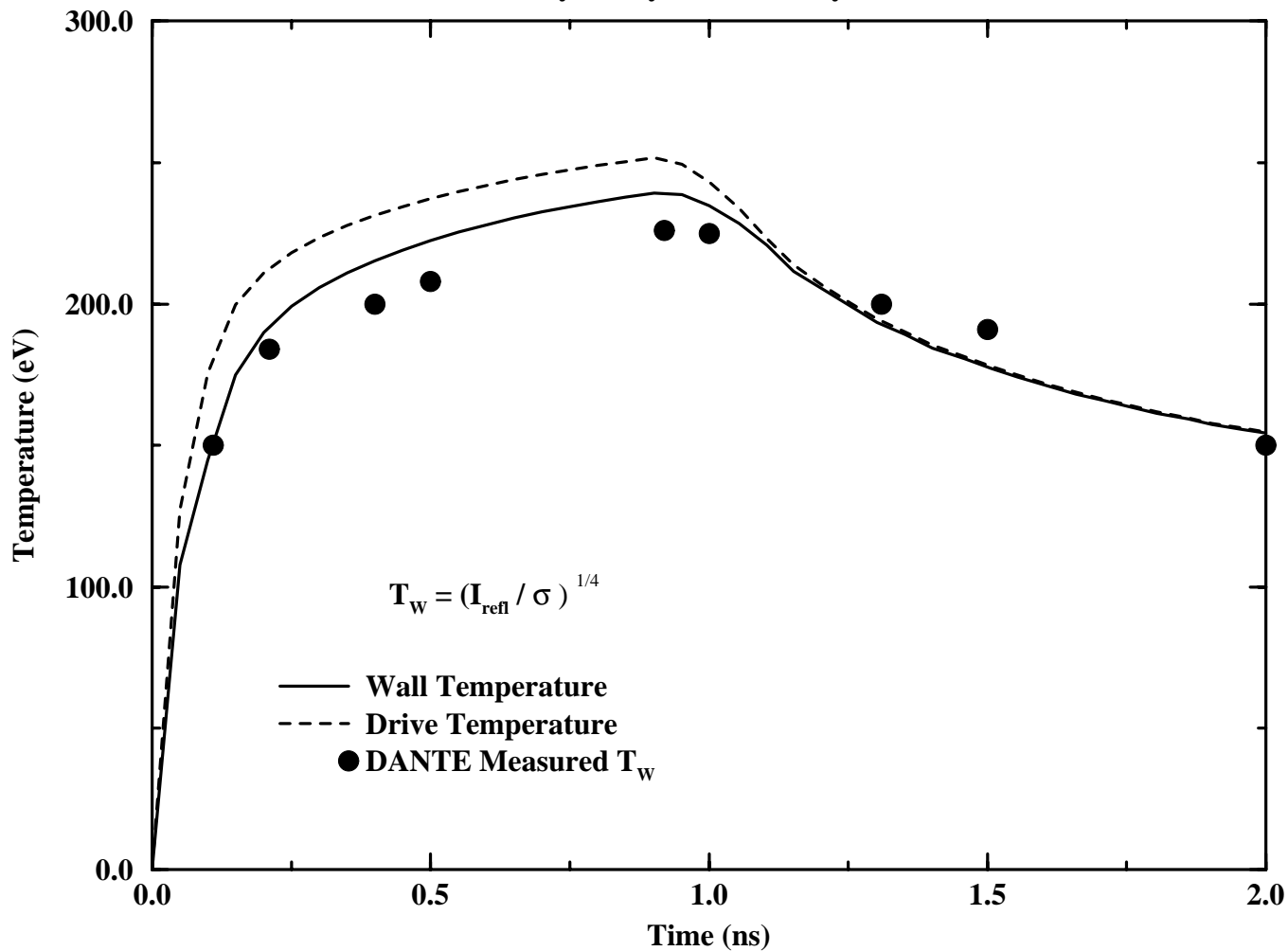


Figure 7. Wall and drive temperatures in Nova hohlraums. Drive and wall temperatures calculated by BUCKY for 150 TW/cm² laser. Wall temperatures are measured by DANTE.

X-Ray Burnthrough of Gold

Nova Experiments versus BUCKY Simulations

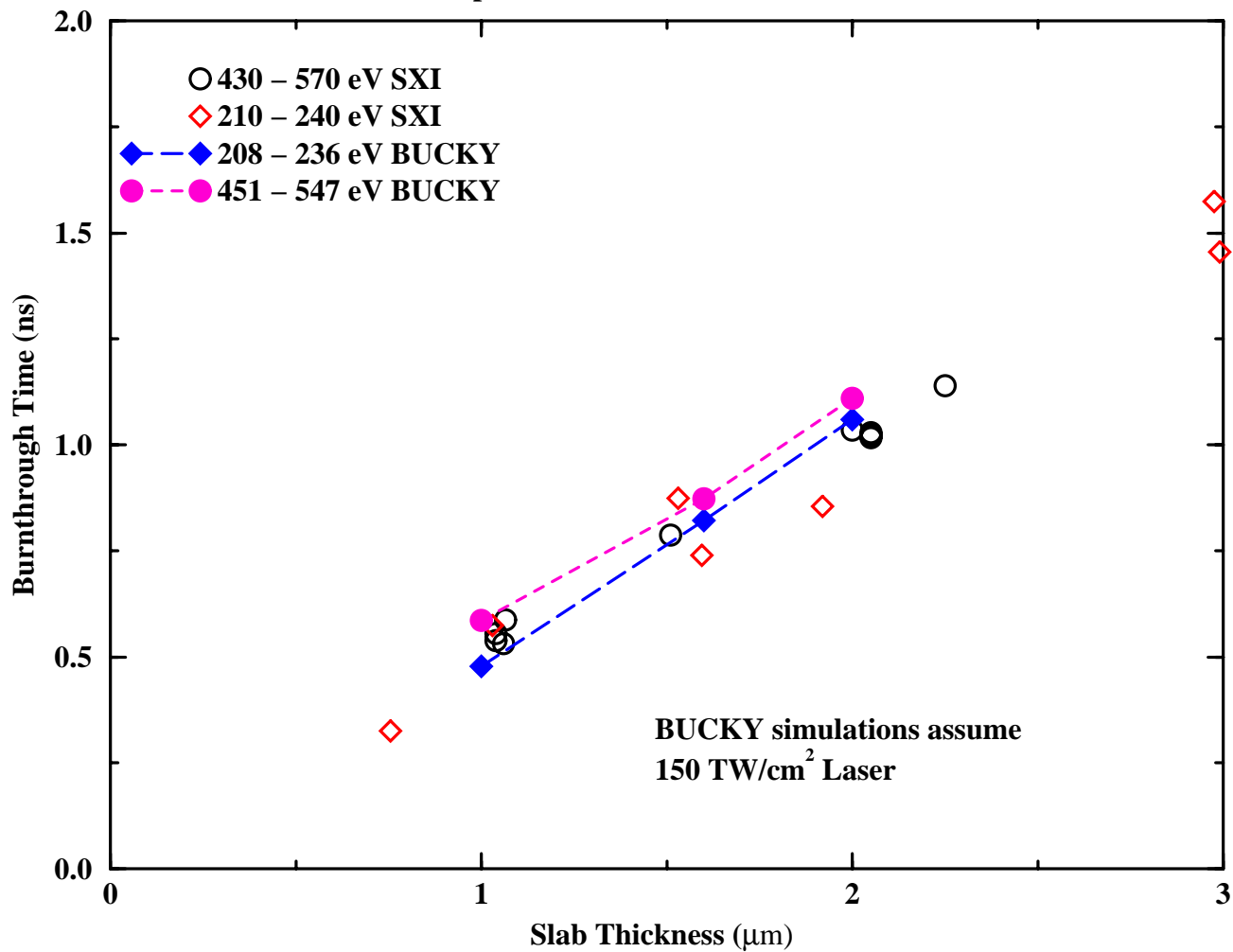


Figure 8. X-Ray burnthrough times in gold versus thickness. Radiation flux is measured by the SXI and calculated with BUCKY at the back of a gold foil in two photon energy bands.

simulations show excellent agreement with the experimental results. This is a confirmation of the radiation diffusion method in BUCKY and the opacities calculated by EOSOPA for use in the simulation of radiation transport in dense high atomic number plasmas.

4. Zeus 2-D Radiation Hydrodynamics Code

The ZEUS-2D radiation-magnetohydrodynamics code [14, 15, 16] has been augmented to add the key capabilities of the University of Wisconsin's 1-D BUCKY code, including

- Multiple materials,
- Multigroup frequency dependence,
- Table lookup of detailed opacities and equations of state.

ZEUS-2D is a two-dimensional, Eulerian-mesh code, written in covariant orthogonal coordinates and solved by finite differences with operator splitting into implicit source and explicit transport steps. The fundamental hydrodynamic equations can be solved alone or with magnetohydrodynamics, radiation, or both. The finite-difference mesh can be modified dynamically, although ZEUS-2D is not an adaptive-mesh code, and the mesh spacing can be varied independently in both dimensions.

The unmodified ZEUS-2D code has been tested on simple radiation diffusion, micro-explosion, and hohlraum test problems, and it appears to be a suitable code upon which to base the desired modifications. Multiple materials have been implemented by including the solution of a separate equation of continuity for each species. The modifications to the difference equations required to add multigroup frequency dependence have been developed and tested in a small auxiliary code, and added to ZEUS-2D. The table lookup subroutines from the BUCKY code for equations of state and opacities have been merged with the ZEUS-2D code.

Testing of the ZEUS-2D has proceeded in four independent areas:

1. multimaterial model.
2. equation of state and opacity table lookup
3. multigroup radiation diffusion
4. hydrodynamics.

ZEUS has a recently added model that tracks the flow of different materials. The flow of different materials in ZEUS-2D is modeled by solving the advection problem separately for each material. The partial pressure in each zone for each material is calculated from the density of that material and the temperature in the zone. The total pressure is just the sum of all the partial pressures in each zone. This is tested by running a standard problem in two ways. The problem, shown in Figures 9 and 10, is a shock driven by a mass density step. In one case, the mass is all a single material. In the other, a second material with identical properties replaces the first material in a region traversed by the shock. In the figures, the short dashed lines are the second material, the long dashes are the first material. The final total mass density profiles are compared, and the relative differences between the two calculations are found to be very small. We will continue testing this model.

The use of realistic equations of state has been added to ZEUS-2D. This has been tested with a problem where temperature boundary conditions are applied to 2 planes bounding a slab and the temperature and densities are allowed to seek equilibrium. The ideal gas model in ZEUS-2D for one run, and the look-up of the same values in a table are used for the other. The results were essentially identical.

Radiation transport via multigroup diffusion has been added to ZEUS-2D. It has been tested with a simple 1-D slab problem, with radiation energy density boundary conditions applied at two surfaces. The energy radiation density relaxes over time to a linear profile as it should.

The hydrodynamics of ZEUS-2D has been used in many astrophysical contexts. We have also tested the use of the code on pure hydrodynamic problems. We have gotten the expected results for hydrodynamic stability problems, where a shock is driven through a rippled high density curtain and becomes Richtmyer-Meshkov unstable. The results of such a simulation are shown in Figure 11. We have plans to perform simulations of shock tube experiments, with the multimaterial model and the table lookup of equations of state.

It has taken us much more effort to reach this stage than we originally thought, so we have just now started testing of the code with integrated benchmarking. We have not been able to obtain results from the MULTI-2D code in Europe that are suitable for benchmarks. We have decided that it makes more sense to compare with experiments when they are available. Gold burnthrough experiments reported below have been used to benchmark the BUCKY code, so we are trying the same for ZEUS-2D. This will test hydrodynamics, radiation transport, and opacity lookups in an integrated way. At the time of this report,

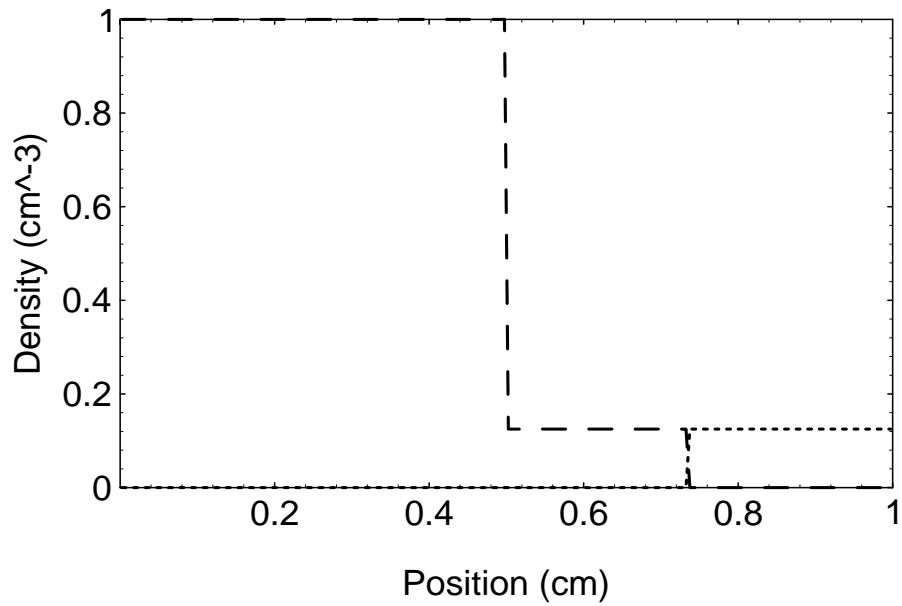
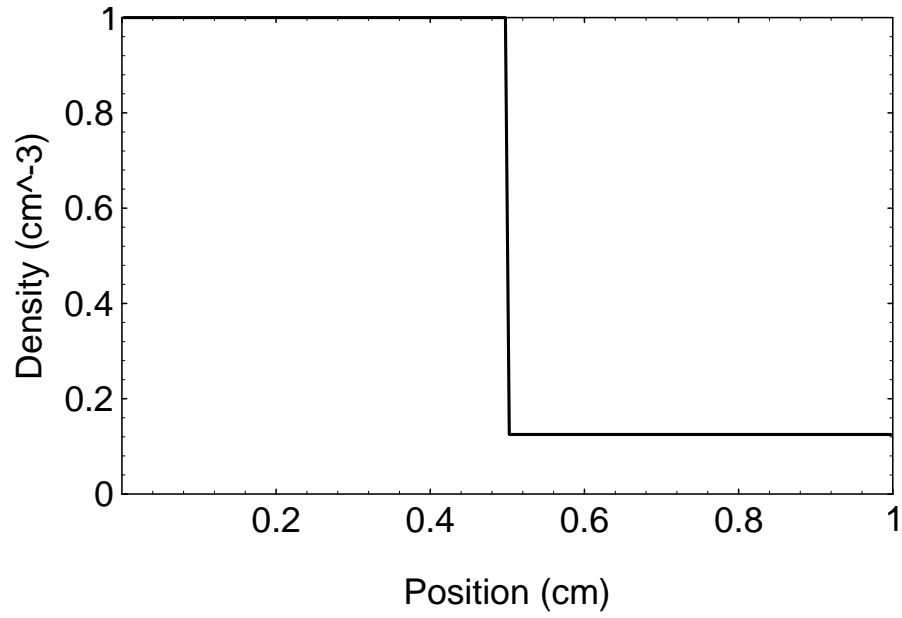


Figure 9. Initial condition of multimaterial test problem. The top figure is the mass density profile for a single material. The second figure shows the mass density split between two materials.

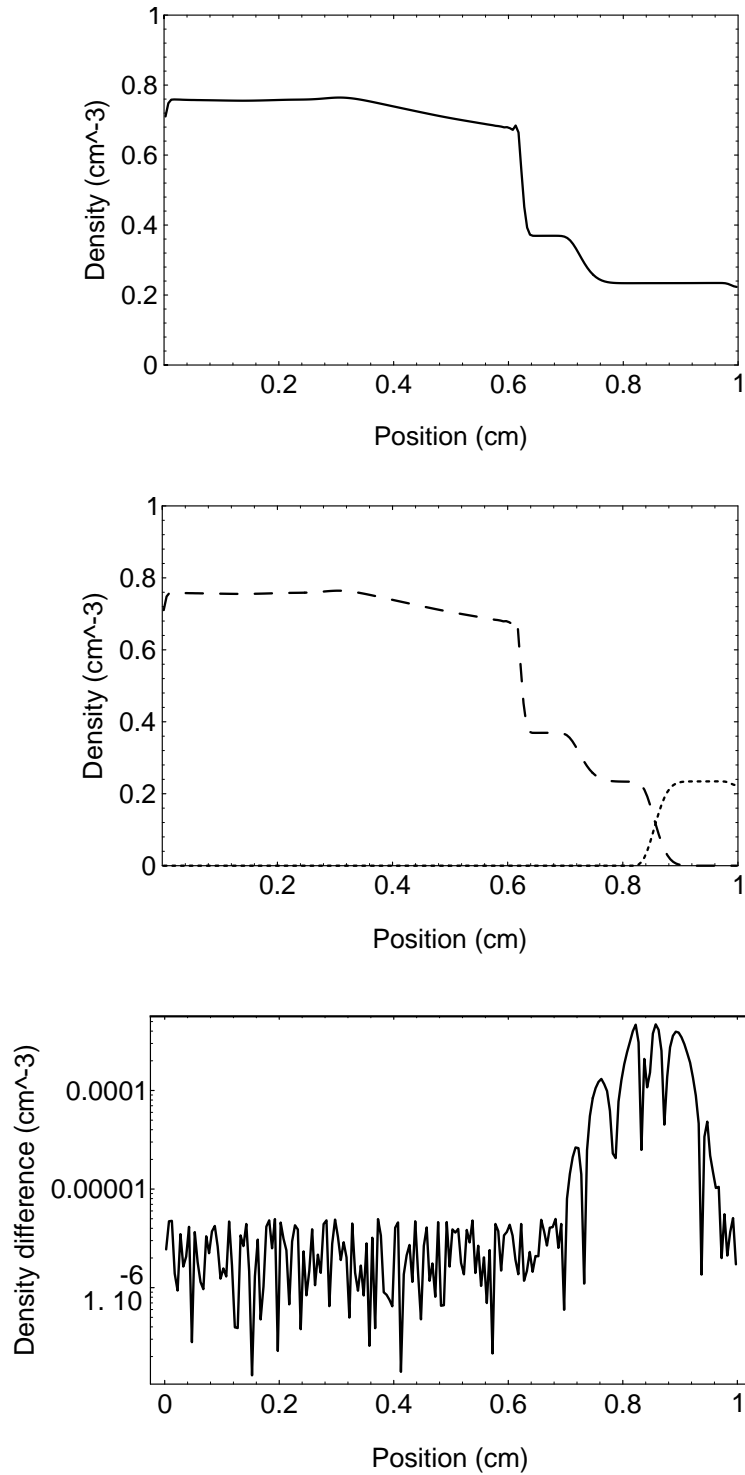


Figure 10. Condition of multimaterial test problem at time after the shock has passed into the second material. The top figure is the mass density profile for a single material. The second figure shows the mass density split between two materials. The bottom figure is the difference in total mass density between the two calculations.

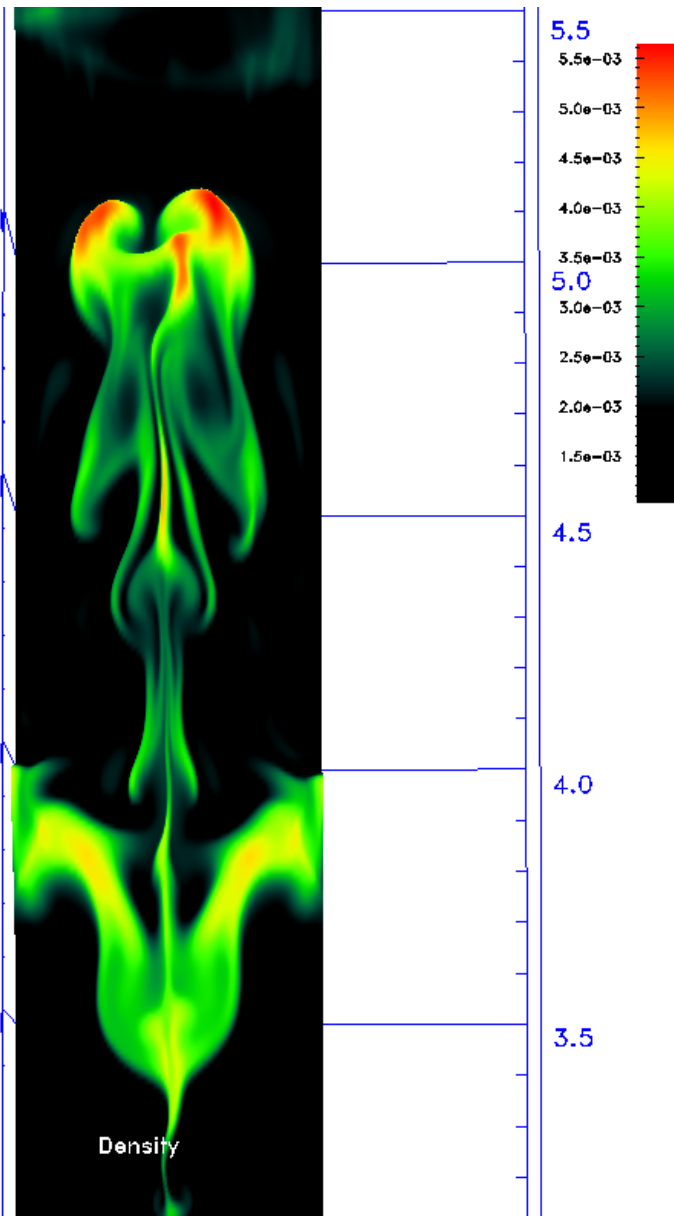


Figure 11. Density contours from ZEUS-2D simulation of shock driven Richtmyer-Meshkov instabilities in a liquid curtain.

we have a bug in these calculations that is as yet unresolved. We will report on these tests at a later date.

5. Experiments Underway at Sandia National Laboratories to Verify Ion Melting Calculations in BUCKY

The ability of BUCKY to model the vaporization of materials by ions has been tested by comparing a simulation with an experiment performed at Sandia National Laboratories. Tim Renk of SNL has irradiated a pure aluminum sample with a fluence ranging from 4 to 8 J/cm² of protons and has measured the melt depth. The experimental layout is shown in Figure 12. The experiment was performed with a light ion diode focusing a beam onto a sample across a distance of 25 cm. The experimental parameters are given in Table 4. The pulse shape for the ions is shown in Figure 13. This is the pulse shape seen at the surface of the sample.

The results of BUCKY simulations of this experiment are shown in Figures 14 through 16. Two simulations were performed, where the proton fluences were 6.8 J/cm² and 3.4 J/cm². The fluences are adjusted by scaling the particle current densities. The shape of the ion current is kept as in Figure 13 and the voltage history is kept exactly as is shown. The vaporized thickness, melted thickness, total damaged thickness and surface temperature are plotted against time for the 6.8 J/cm² fluence simulation in Figure 14. The same are plotted for the 3.4 J/cm² in Figure 15. The temperature, thermal conductivity, heat capacity and deposited ion number density profiles for 3.4 J/cm² protons at 2 μ s after the start of the ion beam are plotted in Figure 16. In this plot, the importance of the temperature dependence of the thermal conductivity of aluminum to these simulations can be seen. The melting temperature of aluminum is 933 K, and molten aluminum has about one half of the thermal conductivity of the solid. This keeps the material molten for a much longer time than one would expect for a constant conductivity. The latent heat of melting is included by adding $\Delta H_{\text{melt}}/T$ to the heat capacity for temperatures greater than the melt temperature. In this plot, one sees that the melt depth is much greater than the ion range, so energy transport via conduction through the molten aluminum is important to the melt depth. As the fluence decreases, the melt depth gets closer to the ion range and conduction in the liquid becomes less important.

The total damage thickness is about the same for 3.4 and 6.8 J/cm²; about 14 μ m. This is consistent with the experiments done at SNL. The high fluence case vaporizes more material, but the vapor is a poor conductor compared to the liquid. So energy in the vapor

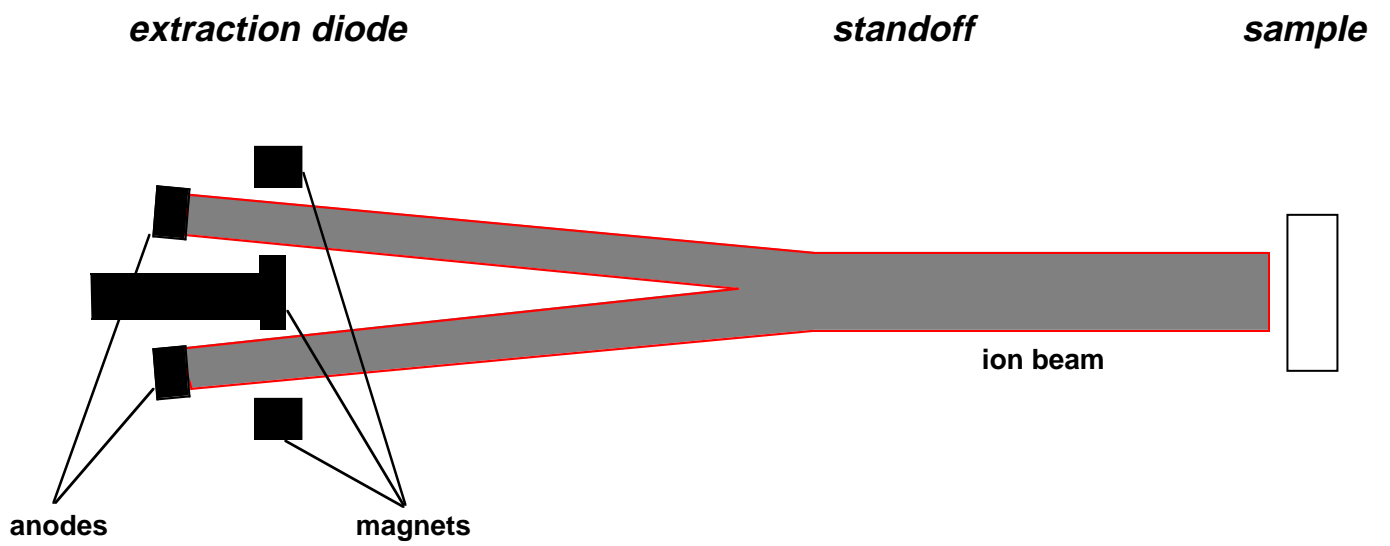


Figure 12. Schematic of SNL ion damage experiment.

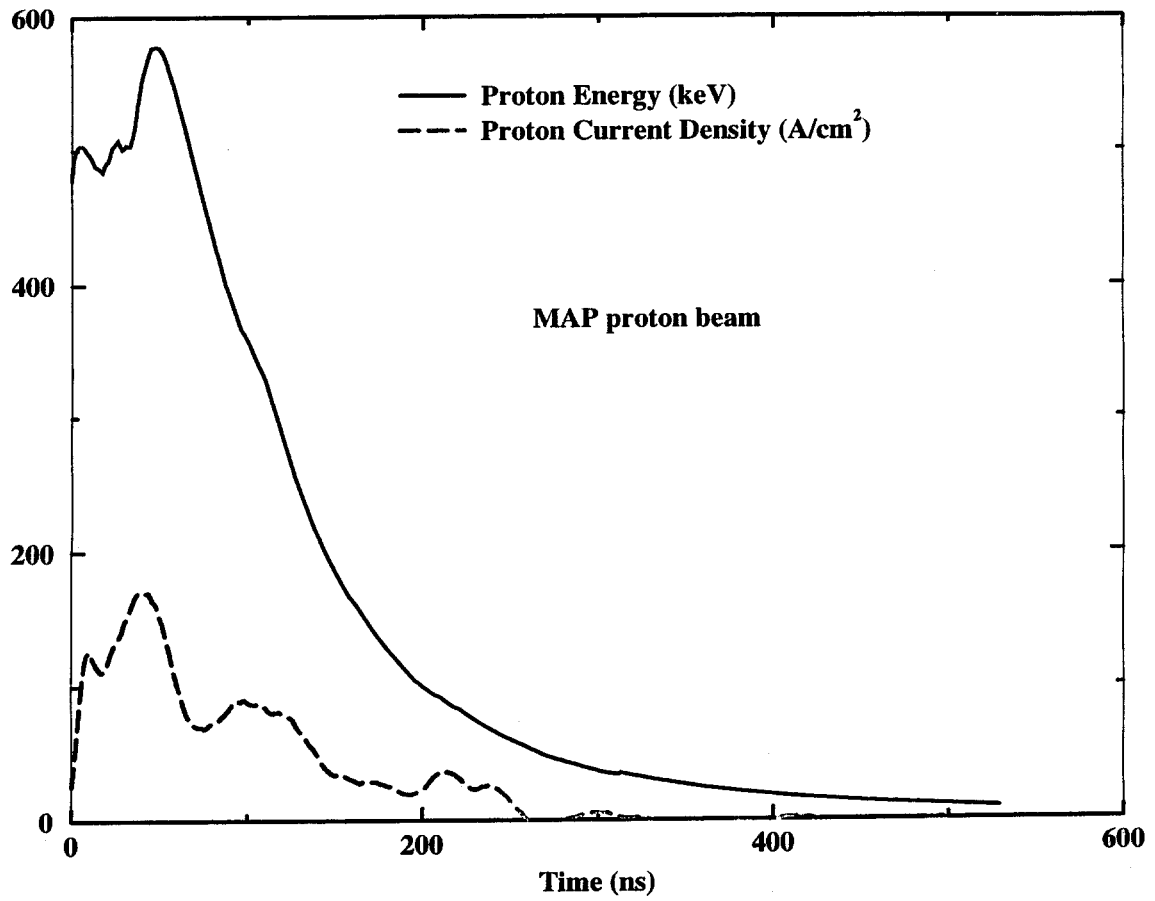


Figure 13. Current density and voltage for ions on surface of aluminum.

Response of Pure Aluminum to MAP Proton Beam

Shot 1499; 6.8 J/cm^2

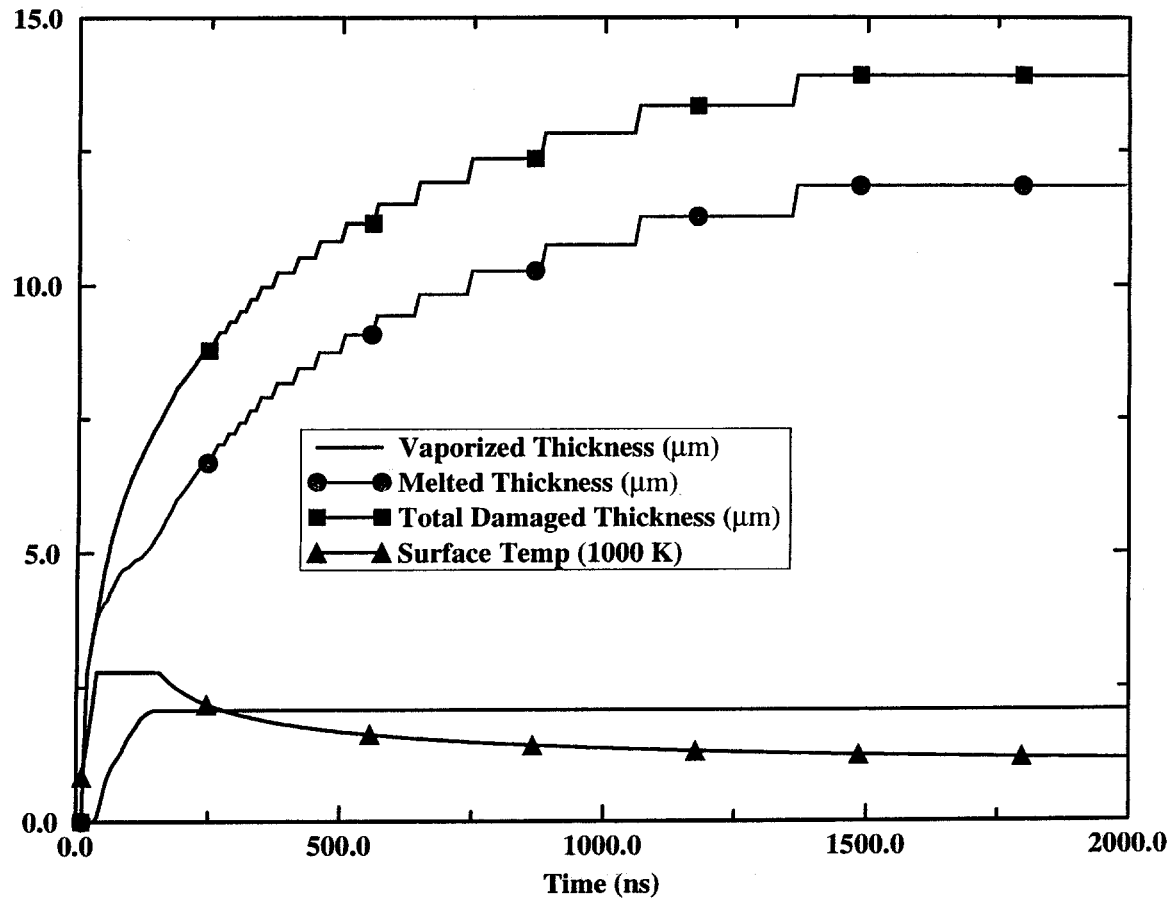


Figure 14. Vaporized thickness, melted thickness, total damaged thickness and surface temperature versus time of pure aluminum irradiated by a 6.8 J/cm^2 proton beam.

Response of Pure Aluminum to MAP Proton Beam

Shot 1499; 3.4 J/cm^2 ; $Z_{\text{solid}} = 0$

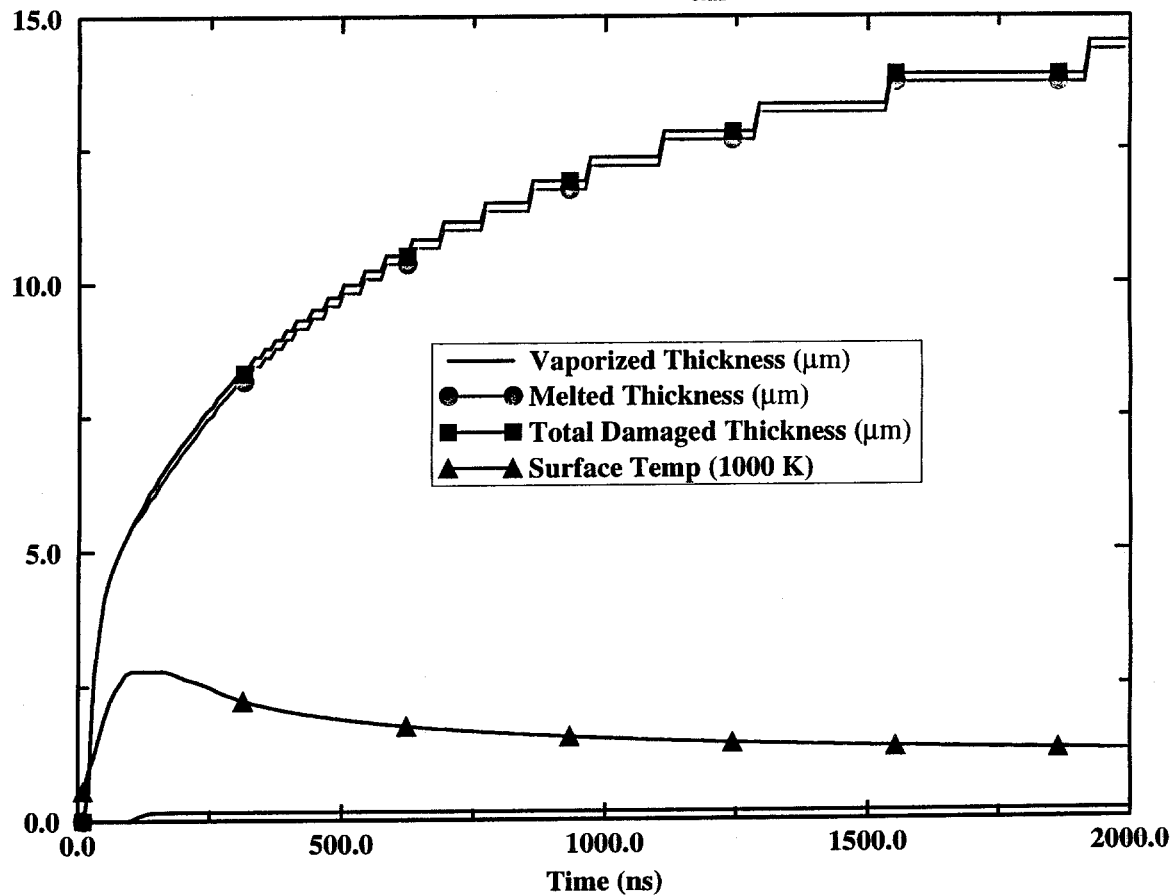


Figure 15. Vaporized thickness, melted thickness, total damaged thickness and surface temperature versus time of pure aluminum irradiated by a 3.4 J/cm^2 proton beam.

Response of Pure Aluminum to MAP Proton Beam

Shot 1499; 3.4 J/cm^2 ; $Z = 0$; Profiles at $2 \mu\text{s}$

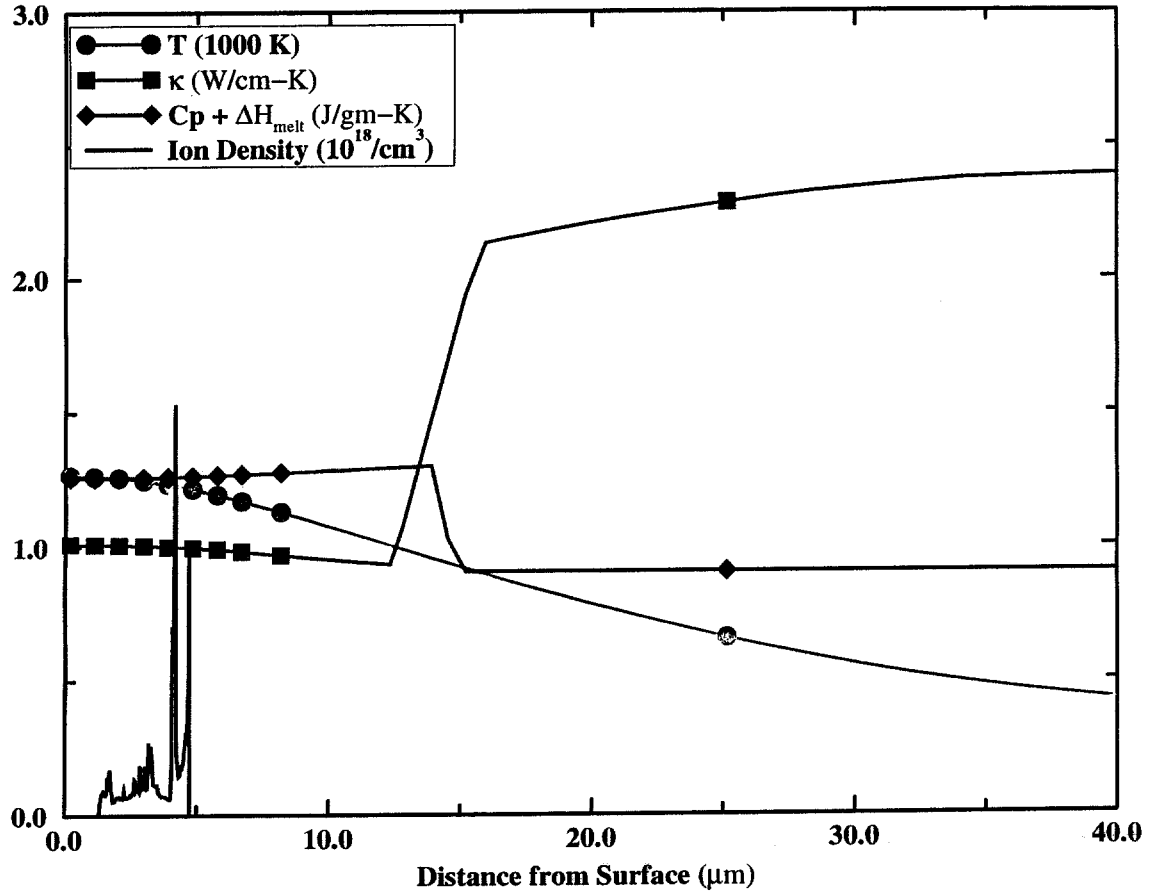


Figure 16. Temperature, thermal conductivity, heat capacity and deposited ion number density profiles for 3.4 J/cm^2 protons at $2 \mu\text{s}$ after start of ion beam. Calculated by BUCKY.

Table 4. Ion Melting Experiment Parameters

Run #	1	2
Peak Energy (keV)	550	550
Peak Current Density (A/cm ²)	65	100
Fluence (J/cm ²)	2.5	4.0
Melt Depth (μm)	8-10	14

is conducted into the material at such a low rate that it does not affect melting. The 3.4 J/cm² case only has a very small amount of vaporization, and the melt depth will drop below that fluence, as the experiments show.

Experiments are now in progress for B₄C and SiO₂. These experiments were planned for last spring, but scheduling and equipment problems prevented them from occurring. The test matrix is shown in Table 5 for these experiments. These will verify BUCKY's predictions for ion damage in NIF target chamber materials.

Acknowledgement

The bulk of this work was supported by Lawrence Livermore National Laboratory under contract #B310594. Part of the work done on the ZEUS code was support by the U.S. Department of Energy on a separate contract. The debris damage experiments are being supported by Sandia National Laboratories.

Table 5. NIF Ion Damage Experiment Parameters

Experimental Matrix from SNL Flashover Diode Experiments

Sample #	1	2	3	4	5	6
Material	SiO ₂	SiO ₂	SiO ₂	B ₄ C	B ₄ C	B ₄ C
Quadrant						
1	0 J/cm ² 1 shot	2 J/cm ² 1 shot	2 J/cm ² 1 shot	2 J/cm ² 1 shot	2 J/cm ² 1 shot	4 J/cm ² 1 shot
2	2 J/cm ² 1 shot	3 J/cm ² 1 shot	2 J/cm ² 5 shots	3 J/cm ² 1 shot	2 J/cm ² 5 shots	4 J/cm ² 5 shots
3	0 J/cm ² 1 shot	2 J/cm ² 1 shot	2 J/cm ² 10 shots	4 J/cm ² 1 shot	2 J/cm ² 10 shots	4 J/cm ² 10 shots
4	maximum 1 shot	maximum 1 shot	2 J/cm ² 15 shots	maximum 1 shot	2 J/cm ² 15 shots	4 J/cm ² 15 shots

References

- [1] J.J. MacFarlane, G.A. Moses and R.R. Peterson, "BUCKY-1 – A 1-D Radiation Transport Code for Simulating Inertial Confinement Fusion High Energy Density Plasmas," University of Wisconsin Fusion Technology Institute Report UWFD-984 (August 1995).
- [2] R.R. Peterson, J.J. MacFarlane, J.F. Santarius, G.A. Moses, "Target Emission and Wall Response: National Ignition Facility Target Area Studies Interim Report for the Period 5/1/95 through 3/31/96" University of Wisconsin Fusion Technology Institute Report UWFD-1008 (April 1996).
- [3] R.R. Peterson, J.J. MacFarlane, J.F. Santarius, P. Wang, G.A. Moses, "The BUCKY and ZEUS-2D Computer Codes for Simulating High Energy Density ICF Plasmas," University of Wisconsin Fusion Technology Institute Report UWFD-1017 (May 1996).
- [4] R.R. Peterson, "Response of National Ignition Facility First Wall Materials to Target X Rays and Debris," University of Wisconsin Fusion Technology Institute Report UWFD-1018 (May 1996).
- [5] R.R. Peterson, J.J. MacFarlane, and P. Wang, "X-Ray and Debris Emission from Direct and Indirect National Ignition Facility Targets," University of Wisconsin Fusion Technology Institute Report UWFD-1016 (May 1996).
- [6] R.R. Peterson, T. Renk, and M. Tobin, "Modeling and Experiment of NIF Target Debris with First Wall Materials," *Bull. Amer. Phys. Soc.* **41**, 1557 (1996) 7S12.
- [7] J. Lindhard and M. Scharff, "Energy Dissipation by Ions in the keV Range," *Phys. Rev.* **124**, 128 (1961).
- [8] H.A. Bethe, *Handbuch der Physik*, Edited by S. Flugge, Springer-Verlag, Berlin, Vol. 24, 273 (1933).
- [9] J.J. MacFarlane and P. Wang, "Numerical Simulation of High Energy Density Plasmas in KALIF Beam-Target Interaction Experiments," University of Wisconsin Fusion Technology Institute Report UWFD-1002 (December 1995).
- [10] J.F. Ziegler, "TRIM-90 The TRansport of Ions in Matter," IBM - Research, Yorktown, New York (1990). Also, J.F. Ziegler, J.P. Biersack, and U. Littmark, "The Stopping and Range of Ions in Solids," Pergamon Press, New York (1985).
- [11] J.L. Porter, et al., "The Albedo of Gold at High Temperatures," ICF Quarterly Report, Lawrence Livermore National Laboratory Report UCRL-LR 105851-94-4 (1994).

- [12] “SESAME: The Los Alamos National Laboratory Equation of State Database,” LANL Report LA-UR-92-3407, edited by S. P. Lyon and J. D. Johnson (1992).
- [13] P. Wang, “EOSOPC - A Code for Computing the Equations of State and Opacities of High Temperature Plasmas with Detailed Atomic Models,” University of Wisconsin Fusion Technology Institute Report UWFDI-933 (December 1993).
- [14] J.M. Stone and M.L. Norman, “ZEUS-2D: A Radiation Magnetohydrodynamics Code for Astrophysical Flows in Two Space Dimensions. I. The Hydrodynamic Algorithms and Tests,” *Astrophysical J. Suppl.* **80**, 753 (1992).
- [15] J.M. Stone and M.L. Norman, “ZEUS-2D: A Radiation Magnetohydrodynamics Code for Astrophysical Flows in Two Space Dimensions. II. The Magnetohydrodynamic Algorithms and Tests,” *Astrophysical J. Suppl.* **80**, 791 (1992).
- [16] J.M. Stone, D. Mihalas, and M.L. Norman, “ZEUS-2D: A Radiation Magnetohydrodynamics Code for Astrophysical Flows in Two Space Dimensions. III. The Radiation Hydrodynamic Algorithms and Tests,” *Astrophysical J. Suppl.* **80**, 753 (1992).